Supporting Information

Regulating Spatial Charge Transfer Over Intrinsically Ultrathin-Carbon-Encapsulated Photoanode Toward Solar Water Splitting

Xiao-Cheng Dai,[a] Ming-Hui Huang,[a] Yu-Bing Li,[a] Tao Li,[a] Bei-Bei Zhang,[a] Yunhui He,[b] Guangcan Xiao,[b] Fang-Xing Xiao [a] *

a. College of Materials Science and Engineering, Fuzhou University, New Campus, Minhou, Fujian Province 350108, China.

b. Instrumental Measurement and Analysis Center, Fuzhou University, Fuzhou, 350002, People's Republic of China.

E-mail address: fxxiao@fzu.edu.cn

Table of Contents

**Fig. S1.** (a) Top-view, (b-d) cross-sectional FESEM images with (f-g) corresponding elemental mapping and (h) EDS results of pristine TNTAs.
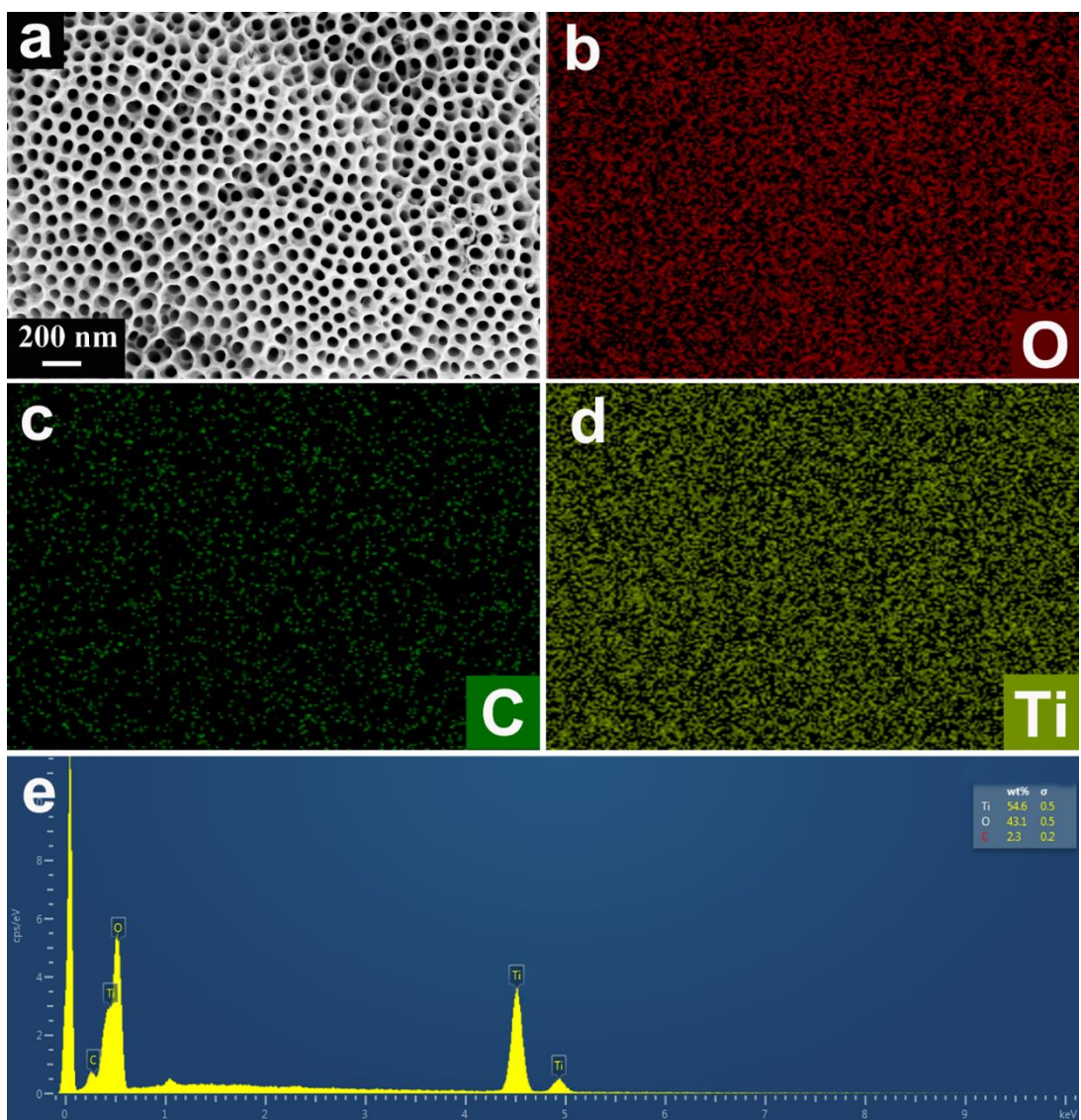
Fig. S2. (a-d) FESEM images with corresponding elemental mapping and (e) EDS results of C-TNTAs.
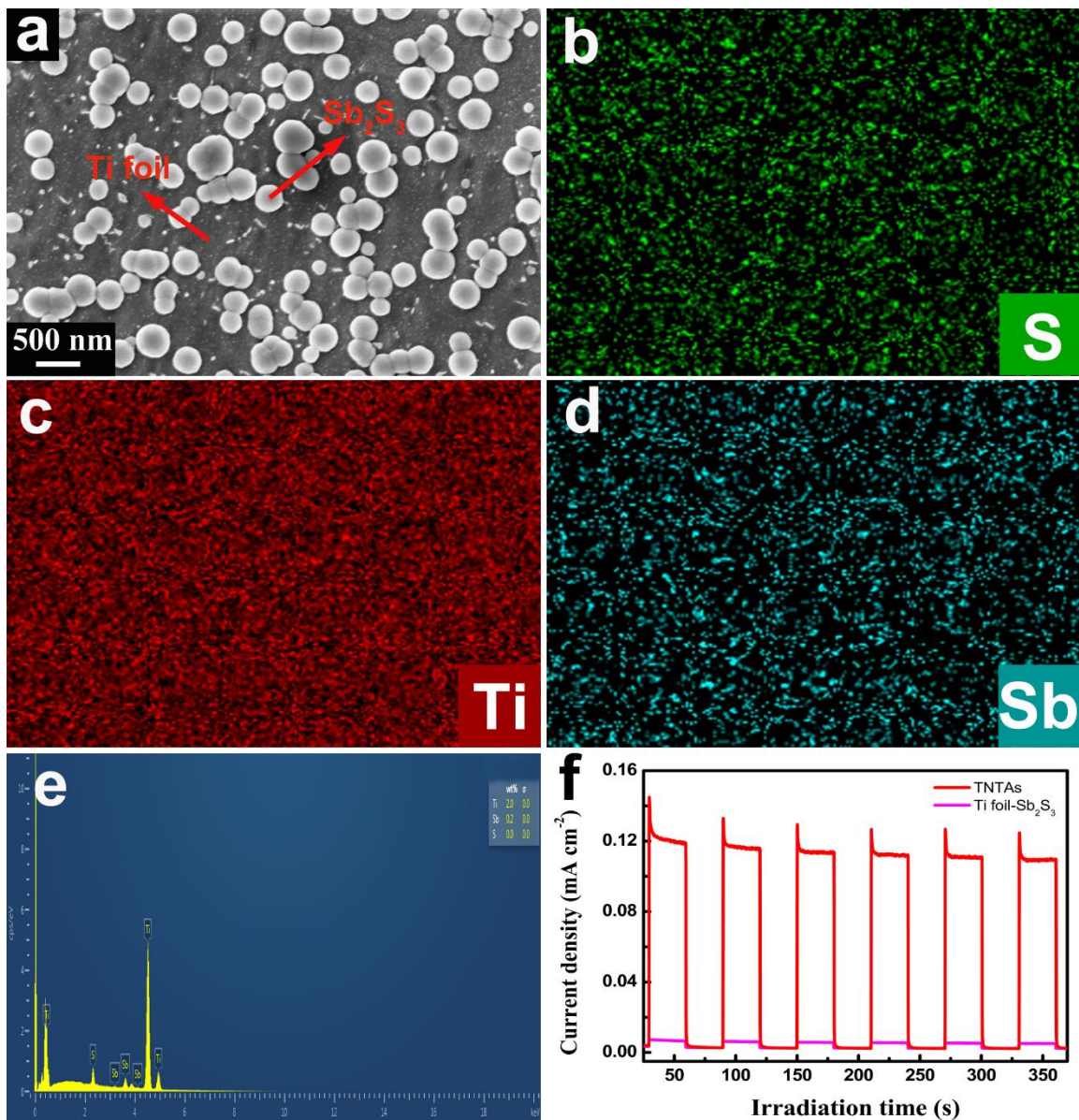
Fig. S3. (a) FESEM image of blank Sb_2S_3 film grown directly on Ti foil with corresponding (b-d) elemental mapping and (e) EDS results, and (f) on-off transient photocurrents of pristine TNTAs and blank Sb_2S_3 under simulated solar light irradiation.

Note: As shown in **Fig. S3(a-e)**, Sb_2S_3 NPs were uniformly deposited on Ti foil without agglomeration and the size of which is analogous to that in nanocomposites. Alternately, note that photocurrent of blank Sb_2S_3 is remarkably lower than TNTAs **(Fig. S3f)** under the same simulated solar light illumination, strongly indicating formation of favorable heterostructure between Sb_2S_3 and TNTAs (TiO_2) is beneficial for improving the separation of photo-induced charge carriers.
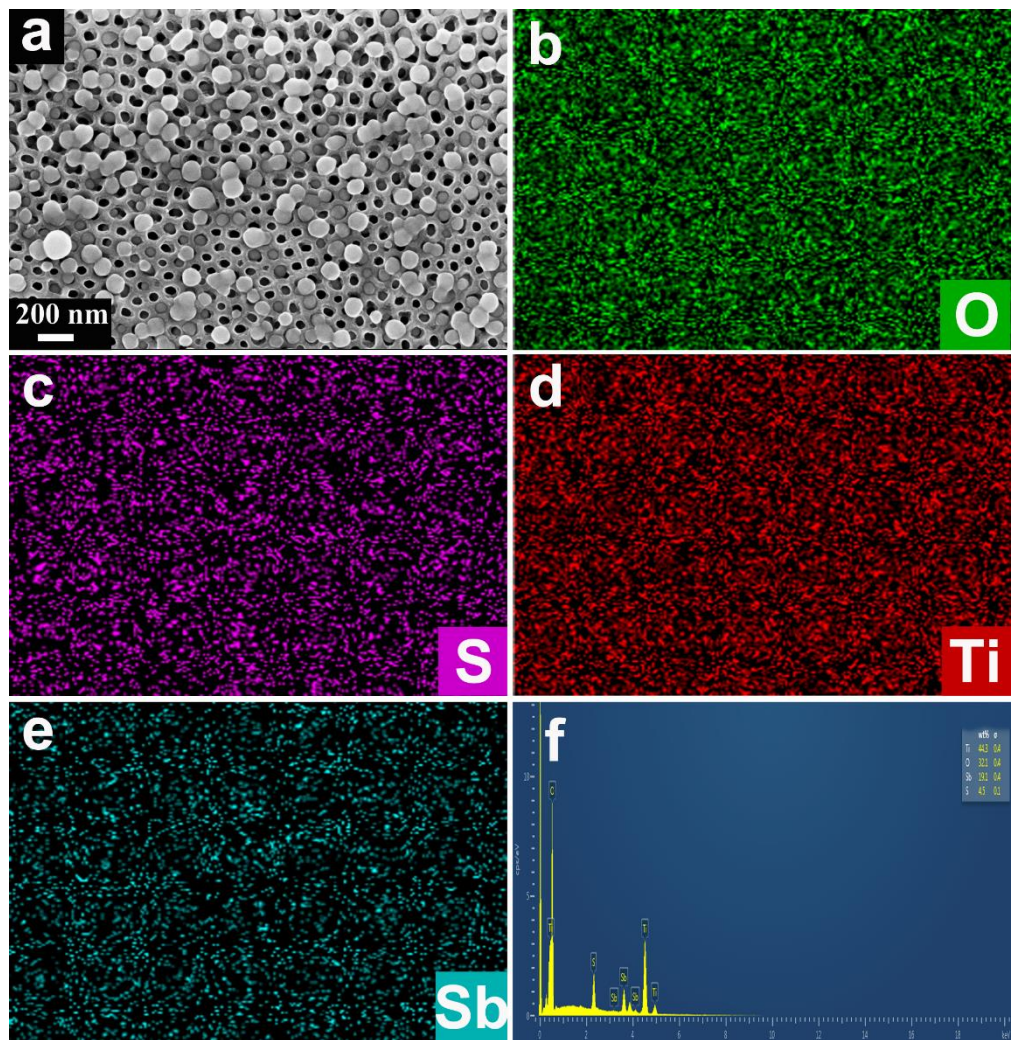
Fig. S4. (a) FESEM image with corresponding (b-e) elemental mapping and (f) EDS result of Sb_2S_3-TNTAs.
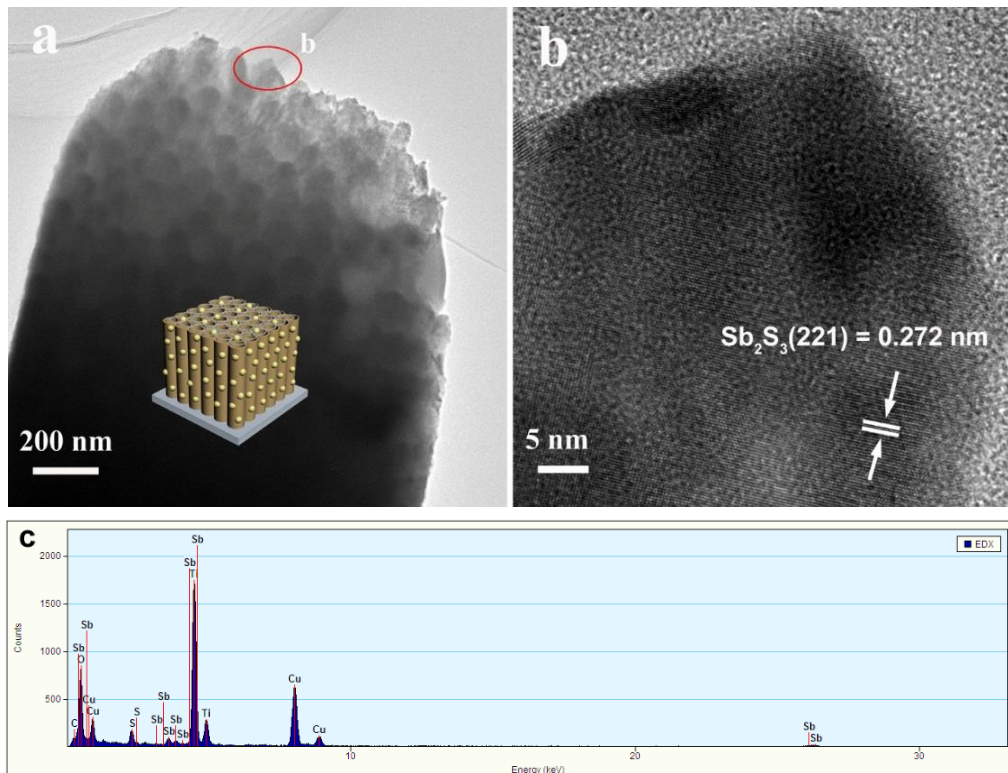
Fig. S5. (a) TEM, (b) HRTEM images of C-Sb_2S_3-TNTAs ternary heterostructure and (c) EDS result of C-Sb_2S_3-TNTAs. Inset shows the corresponding model of C-Sb_2S_3-TNTAs in (a).
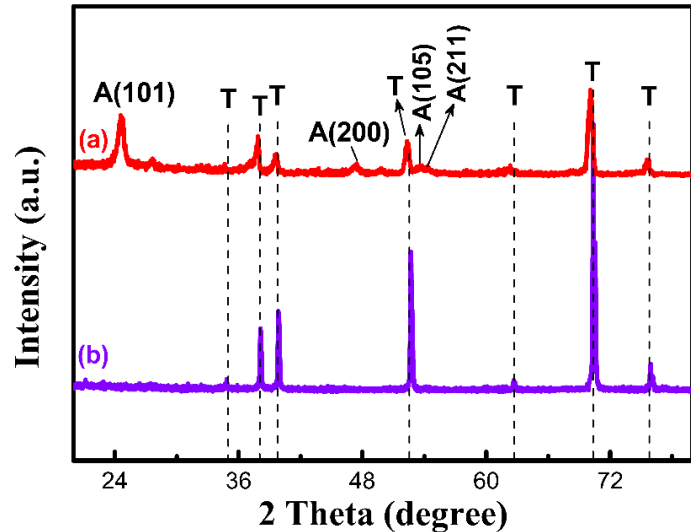
Fig. S6. XRD patterns of (a) C-Sb_2S_3-TNTAs and (b) blank Sb_2S_3 film directly grown on Ti foil. (A: Anatase; T: Ti).

Note: Deposition amount of Sb_2S_3 on blank Ti foil is same to that in Sb_2S_3-TNTAs and C-Sb_2S_3-TNTAs nanocomposites. Apparently, only the diffraction peaks of metal Ti were seen in the XRD pattern of blank Sb_2S_3 film, which might be ascribed to the fact that Sb_2S_3 peaks were shielded by the primary diffraction peaks of anatase TiO_2 and Ti foil owing to its low loading amount.
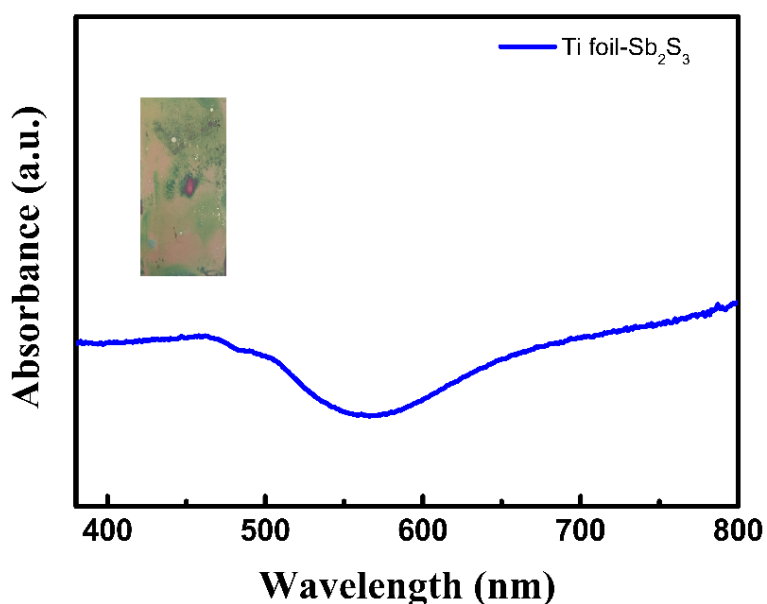
Fig. S7. UV-vis diffuse reflectance spectra (DRS) of Sb_2S_3 film directly grown on Ti foil with corresponding photograph in the inset.

Note: It is obvious that absorption band edge of Sb_2S_3 film directly grown on Ti foil locates at *ca.* 623.4 nm which is in line with those of Sb_2S_3-TNTAs and C-Sb_2S_3-TNTAs, indicative of conspicuously enhanced light absorption of Sb_2S_3-TNTAs and C-Sb_2S_3-TNTAs afforded by Sb_2S_3 photosensitization.
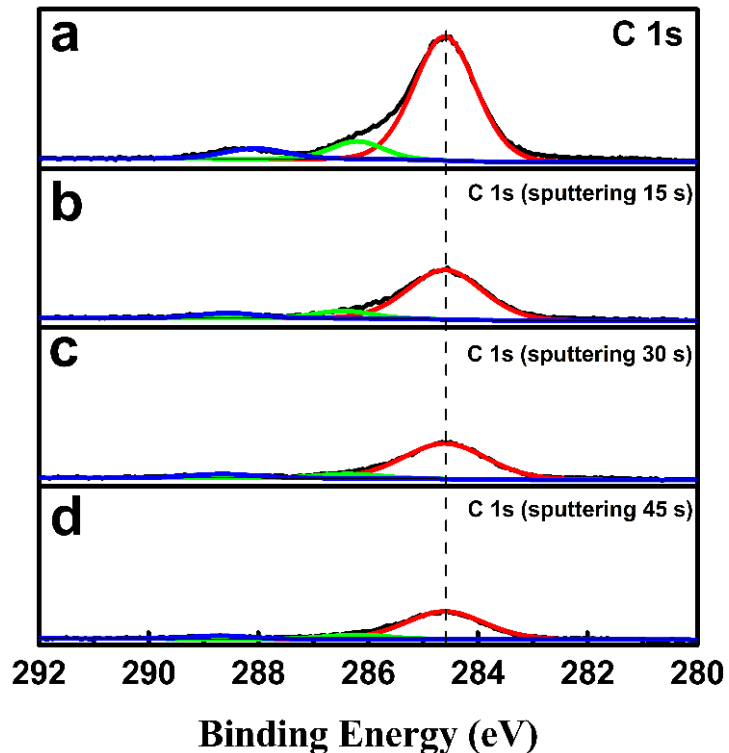
Fig. S8. High-resolution C 1s spectra of C-TNTAs (a) without sputtering and (b-d) after sputtering for different time (15, 30, 45 s).

Note: Substantial C1s signal can still be probed when sputtering time increases from 15 to 45 s, by which surface layer of C-TNTAs was removed and bulk phase was exposed. The result strongly substantiates ultra-thin carbon encapsulation on the surface.
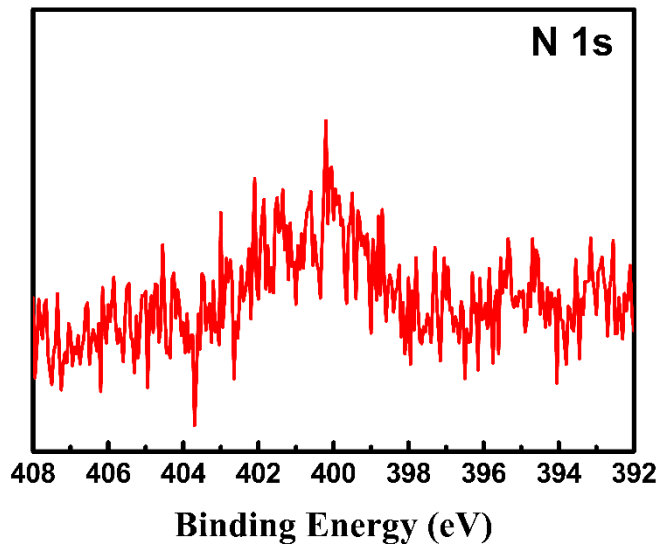
Fig. S9. High-resolution N 1s spectrum of C-Sb$_2$S$_3$-TNTAs.
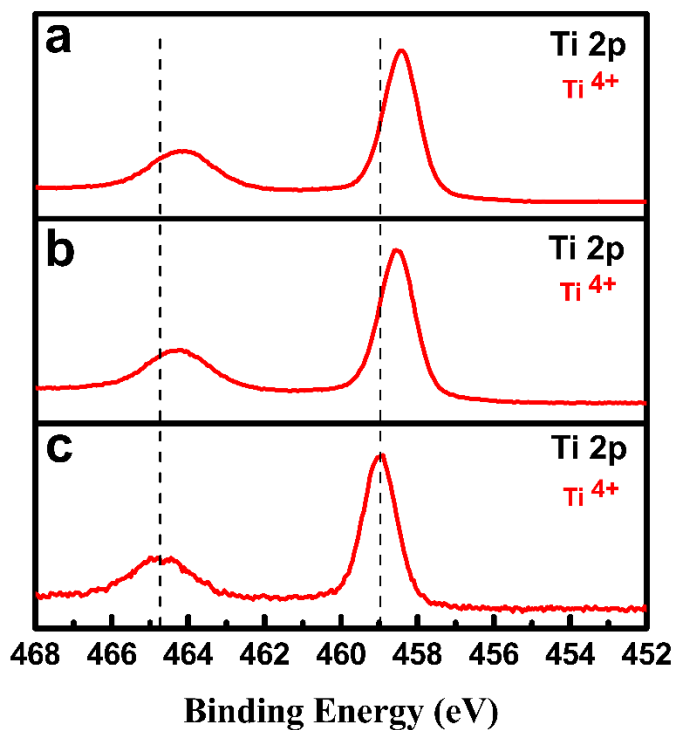
Fig. S10. High-resolution Ti 2p spectra of (a) pristine TNTAs, (b) C-TNTAs and (c) Sb$_2$S$_3$-TNTAs.

Note: Pronounced positive B.E. shift in the high-resolution Ti 2p spectra of C-TNTAs and Sb$_2$S$_3$-TNTAs compared with pristine TNTAs implies the synergistic interaction of ingredients and substrate.

Table S1. Chemical bond species *vs.* B.E. for different photoelectrodes.

| *Element*	*TNTAs*	*C-TNTAs*	*Sb₂S₃-TNTAs*	*C-Sb₂S₃-TNTAs*	*Chemical Bond Species*
C 1s A	284.6	284.6	284.6	284.6	C-C/C-H
C 1s B	286.2	286.2	286.4	286.6	C-OH/C-O-C[S1]
C 1s C	288.1	288.1	288.5	288.8	Carboxyl (-COO$^-$)[S2]
O 1s A	529.6	529.9	530.0	530.0	Lattice Oxygen
O 1s B	531.5	531.6	N.D.	N.D.	Ti-OH[S3]
O 1s C	532.6	532.9	N.D.	N.D.	O–C–O[S4]
Ti 2p$_{3/2}$	458.4	458.5	458.9	459.0	Anatase (4$^+$)[S5]
Ti 2p$_{1/2}$	464.1	464.2	464.7	464.7	Anatase (4+)
Sb 3d$_{5/2}$	N.D.	N.D.	529.8	530.0	Sb^{3+}[S6]
Sb 3d$_{3/2}$	N.D.	N.D.	539.1	538.8	Sb^{3+}
S 2p$_{3/2}$	N.D.	N.D.	161.3	161.2	S^{2-}[S7]
S 2p$_{1/2}$	N.D.	N.D.	162.5	162.4	S^{2-}

N.D.: Not Detected.

Note: Some typical chemical bond species, such as carboxylate, lattice oxygen, and Ti-OH in C-Sb₂S₃-TNTAs show concurrent substantial shifts in B.E., thus once again indicating the synergistic interaction of *in-situ* encapsulated carbon layer, Sb₂S₃ nanocrystals and TNTAs substrate.
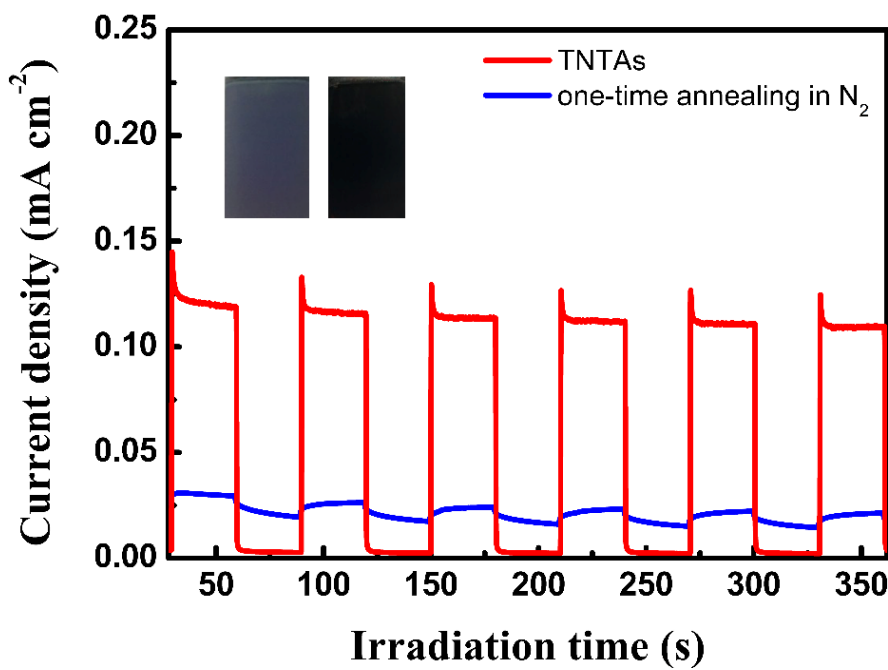
Fig. S11. On-off transient photocurrents of blank TNTAs and one-time-annealed (in N_2) C-TNTAs with corresponding photographs in the inset (left to right: TNTAs, one-time annealing C-TNTAs).

Note: Excessive carbon remaining on the TNTAs after first annealing treatment in N_2 seriously affects the light absorption of TNTAs leading to lower photocurrent density of C-TNTAs in comparison with blank TNTAs. Therefore, it is highly desirable to finely tune the carbon amount on the TNTAs for boosting the PEC performances of C-TNTAs.
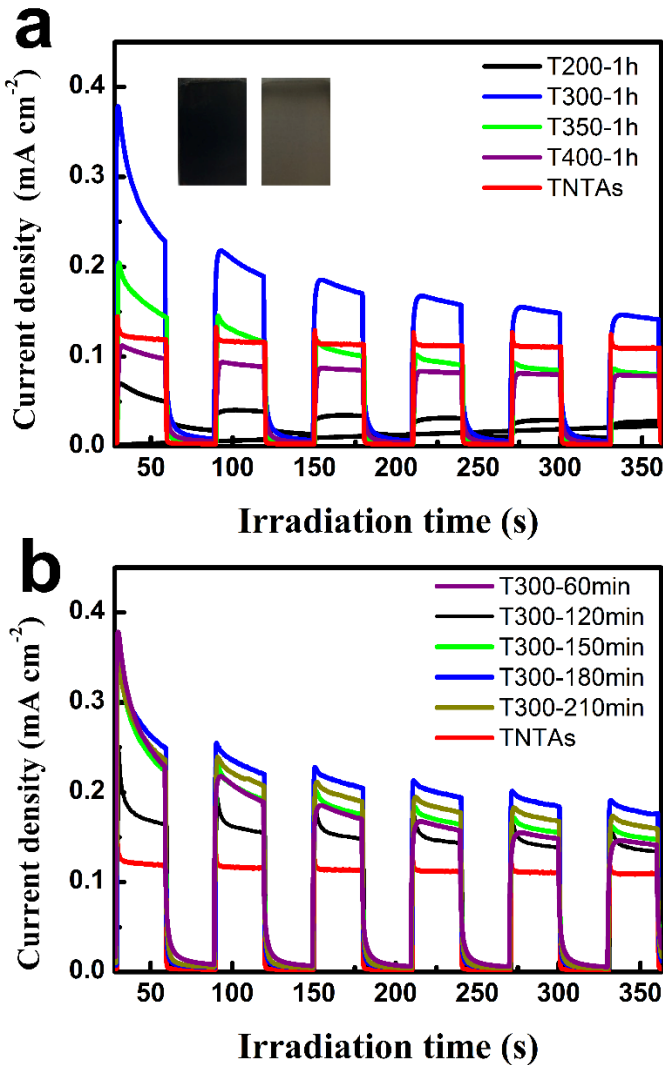
Fig. S12. On-off transient photocurrent of C-TNTAs after second-annealing in air by modulating the (a) annealing temperature (t=1 h) and (b) time (T=300 °C). Photographs of C-TNTAs subjected to one-time-annealing (left graph) and second-annealing (right graph) treatments were displayed in the inset of (a).

Note: Fig. S12a shows that photocurrent of C-TNTAs increases with increasing second-annealing temperature (in air) from 200 to 300 °C and then decreases upon further boosting the temperature. Moreover, it was unveiled in **Fig. S12b** that calcination time also considerably influences the photocurrent of C-TNTAs (T=300 °C) which gradually increases with increasing the annealing time from 60 to 180 min and subsequently, it decreases upon prolonging the annealing time to 210 min. Obviously, high temperature or too long annealing time leads to over-combustion of carbon on the TNTAs, while insufficient annealing temperature and time give rise to over-coverage of carbon on the TNTAs. Consequently, based on the above systematic investigation, optimal experimental conditions (annealing temperature in air and annealing time) for favorable ultra-thin carbon encapsulation on TNTAs have been determined, that is, 300 °C and 180 min.
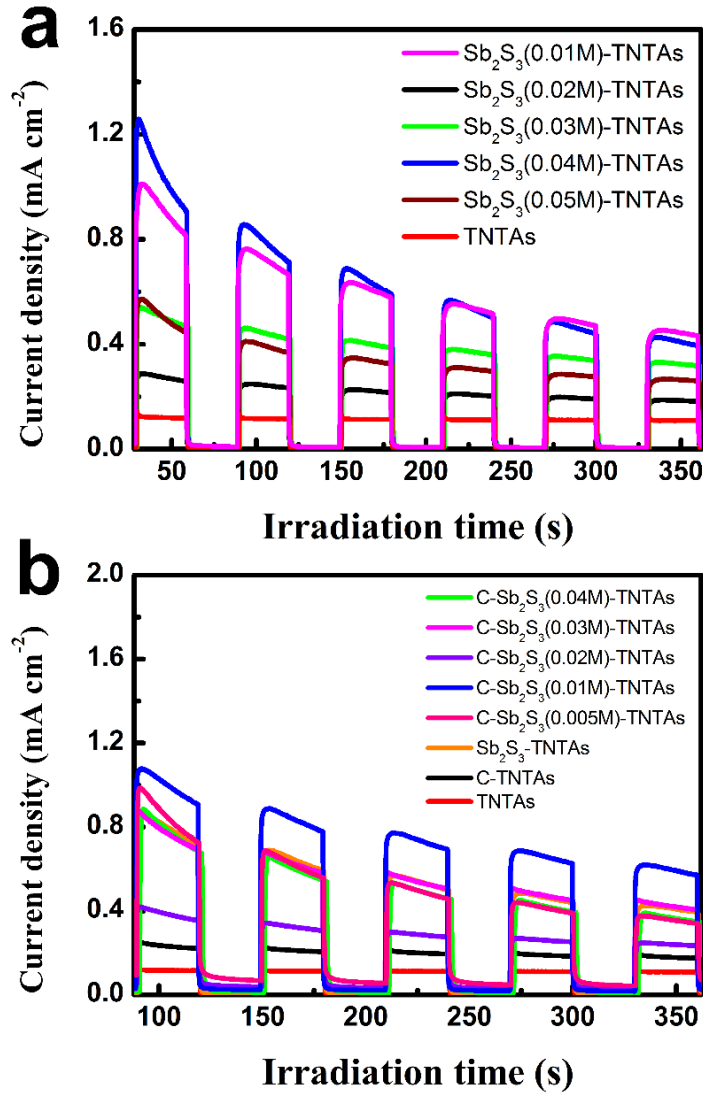
Fig. S13. On-off transient photocurrent of (a) Sb_2S_3-TNTAs and (b) C-Sb_2S_3-TNTAs with different deposition amount of Sb_2S_3 nanocrystals. Deposition amount of Sb_2S_3 on the TNTAs or C-TNTAs substrate was tuned by changing the concentration of $SbCl_3$ precursor.

Note: Fig. S13a shows that photocurrent density of Sb_2S_3-TNTAs increases with increasing the $SbCl_3$ precursor concentration from 0.01 M to 0.05 M, among which Sb_2S_3(0.04 M)-TNTAs demonstrates the optimal photocurrent density. As unveiled in **Fig. S13b**, photocurrent density of C-Sb_2S_3-TNTAs gradually increases with increasing the $SbCl_3$ precursor concentration from 0.005 M to 0.01 M and then decreases upon further increasing the concentration to 0.04 M. Obviously, too large Sb_2S_3 deposition amount retards the light absorption and photo-excitation of TNTAs as well as efficacious photogenerated charge carriers transfer. Consequently, optimal experimental conditions for favorable Sb_2S_3 deposition on the C-TNTAs substrate have been determined (*i.e.*, 0.01 M $SbCl_3$).
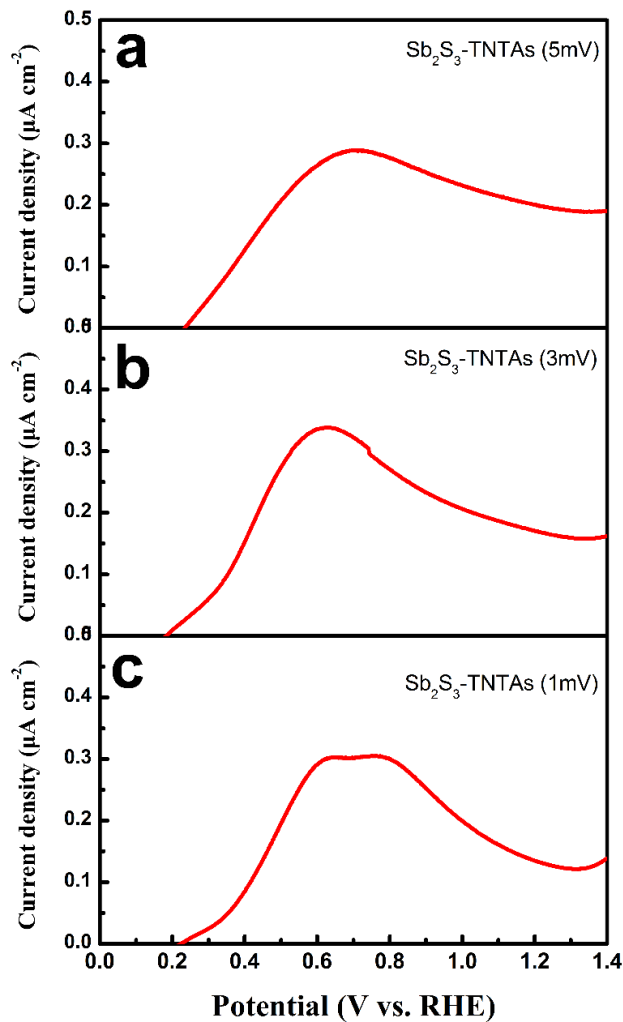
Fig. S14. LSV results of Sb$_2$S$_3$-TNTAs collected at different scan rate (a) 5 mV, (b) 3 mV, and (c) 1 mV under visible light irradiation (λ>420 nm).

**Note:** LSV curves of Sb$_2$S$_3$-TNTAs always exhibit a peak at around 0.8 V vs. RHE under different scan rate under visible light irradiation and this strongly evidences the peak observed in the LSV result of C-Sb$_2$S$_3$-TNTAs arises from partial oxidation of Sb$_2$S$_3$.
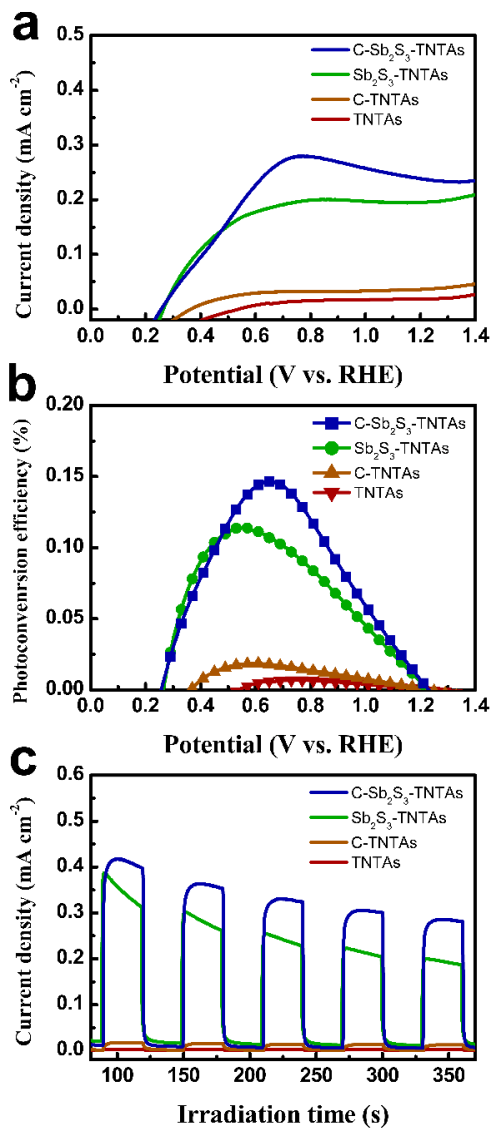
Fig. S15. (a) LSV results (5 mV s^{-1}) (b) ABPE results, and (c) transient photocurrent responses of different photoanodes at an applied potential of 1.23 V vs. RHE under visible light irradiation (λ>420 nm).

Note: It is clearly seen in **Fig. S15a** that photocurrent of TNTAs is almost zero under visible light irradiation (λ>420 nm) due to the wide bandgap of TiO$_2$ (*ca*. 3.2 eV). Notably, photocurrent of C-TNTAs is larger than pristine TNTAs and this confirms the role of ultrathin encapsulated carbon layer in ameliorating charge separation and transfer. Moreover, photocurrents of Sb$_2$S$_3$-TNTAs and C-Sb$_2$S$_3$-TNTAs were substantially boosted compared with TNTAs and C-TNTAs, once again evidencing Sb$_2$S$_3$ markedly favors the light absorption of TNTAs for visible light harvesting as well as its capability to form favorable heterostructure with TNTAs substrate. Consistently, ABPE (**Fig. S15b**) and transient photocurrent (1.23 V vs. RHE) results (**Fig. S15c**) points to the same conclusion, which agrees well with their PEC water splitting performances under simulated solar light irradiation.
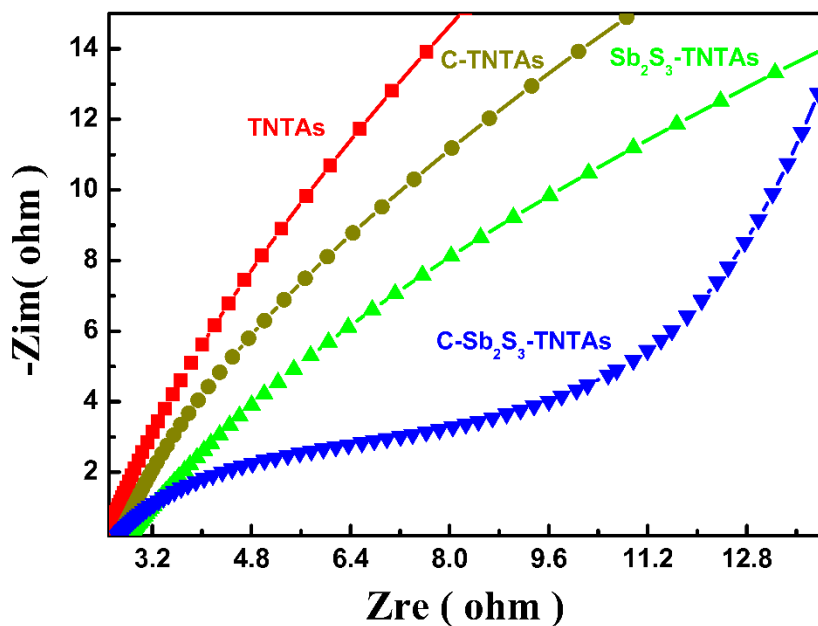
**Fig. S16.** EIS results of different photoanodes in dark.

Table S2. Fitted EIS results of different photoanodes under visible light irradiation based on the equivalent circuit.

| Photoanodes	R_s/ohm	R_{ct}/ohm	CPE/(F·cm^{-2})	Zw/ohm
TNTAs	2.87	11.9	6.384	5.132
C-TNTAs	2.906	10.84	4.513	3.211
Sb$_2$S$_3$-TNTAs	2.019	7.703	3.668	4.183
C- Sb$_2$S$_3$-TNTAs	0.91	2.36	1.817	3.886

Note: As shown in **Table S2**, R_{ct} values were extracted from the semicircle by fitting it according to a simple equivalent circuit composed of a series resistance (**Fig.5d**, inset). Apparently, C-Sb$_2$S$_3$-TNTAs demonstrated the smallest R_{ct} value in comparison with other counterparts, indicative of the lowest charge transfer resistance in the interfacial region.
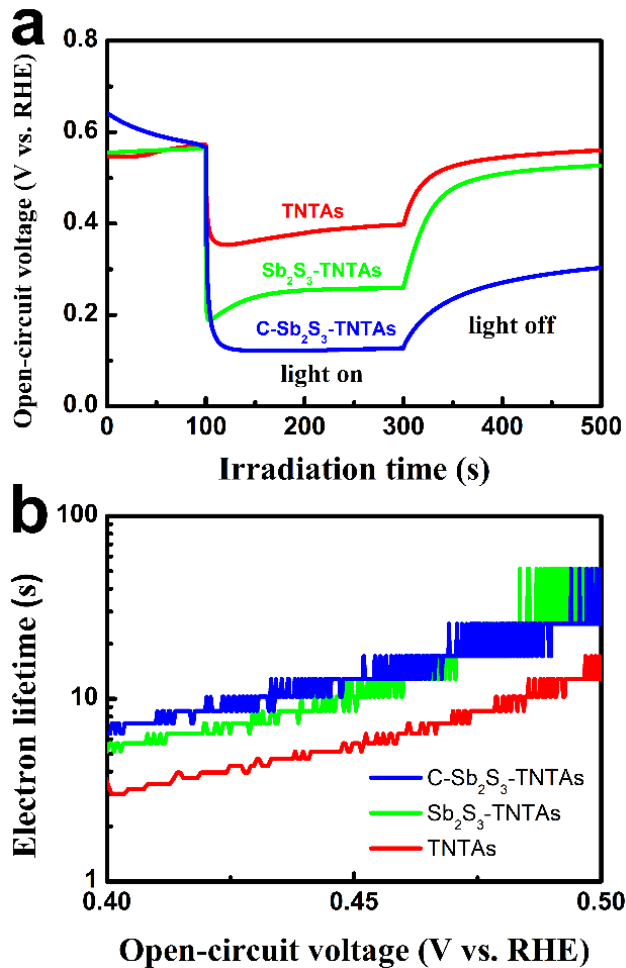
Fig. S17. (a) Open-circuit voltage decay (OCVD) profiles of pristine TNTAs, Sb$_2$S$_3$-TNTAs, and C-Sb$_2$S$_3$-TNTAs with corresponding (b) average electron lifetime (τ_n) calculated based on the OCVD results.
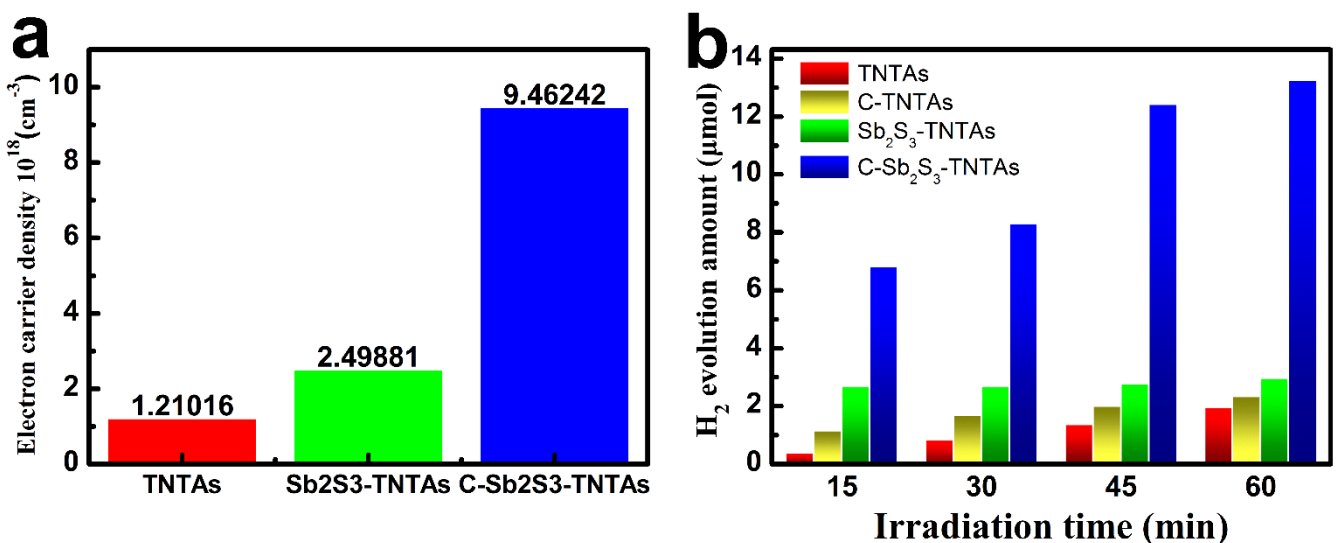

Fig. S18. (a) Charge carrier density (Nd) of different photoanodes calculated by the Mott-Schottky results, and (b) H$_2$ evolution amount under a bias of 1.23 V vs. RHE in Na$_2$SO$_4$ (0.5 M, pH=6.69) aqueous solution under continuous simulated solar light irradiation (100 mW/cm^2, AM 1.5G).
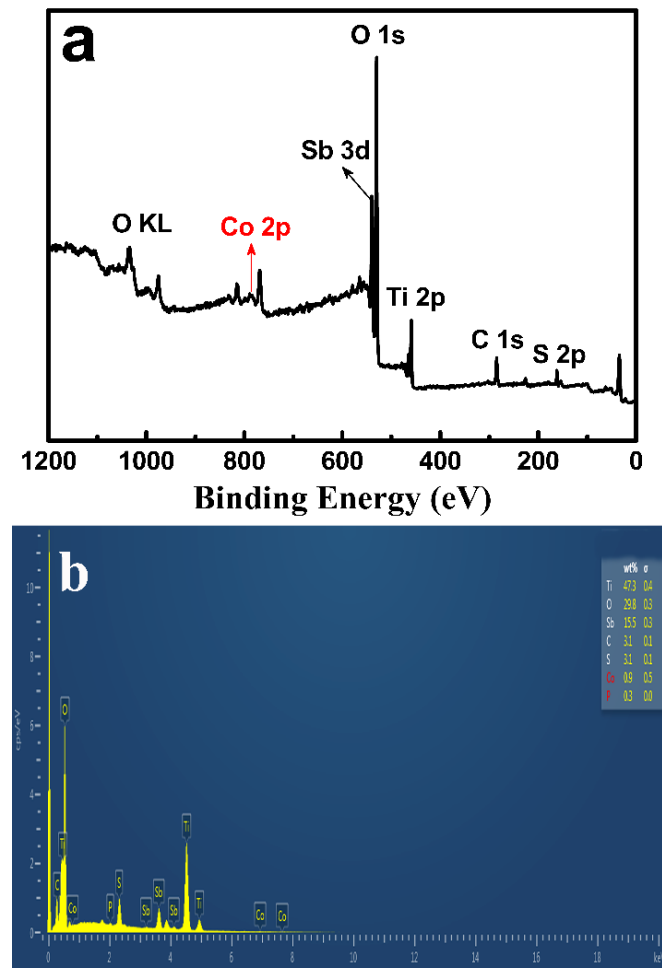
Fig. S19. (a) Survey spectra and (b) EDS result of C-Sb$_2$S$_3$-TNTAs/Co-Pi prepared by photo-assisted electrodeposition (PED) method.
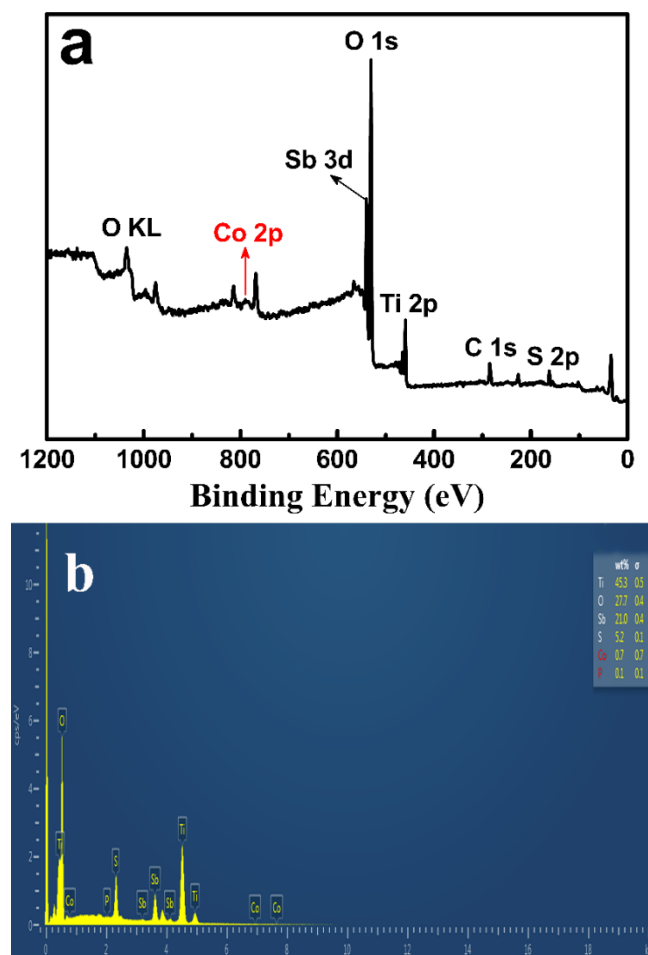
Fig. S20. (a) Survey spectra and (b) EDS result of C-Sb2S3-TNTAs/Co-Pi prepared by direct electrochemical deposition (ED) method.
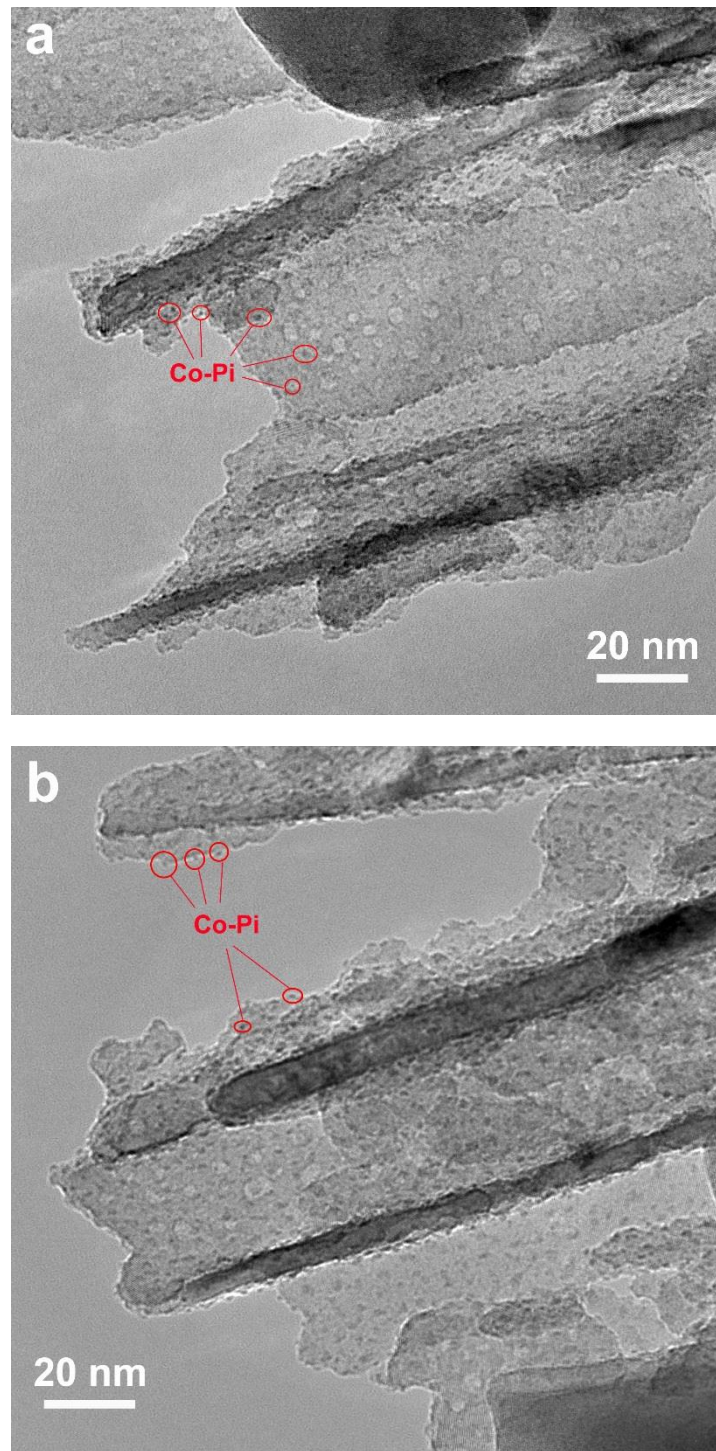
Fig. S21. TEM images of C-Sb$_2$S$_3$-TNTAs with Co-Pi deposition by (a) PED and (b) ED methods.
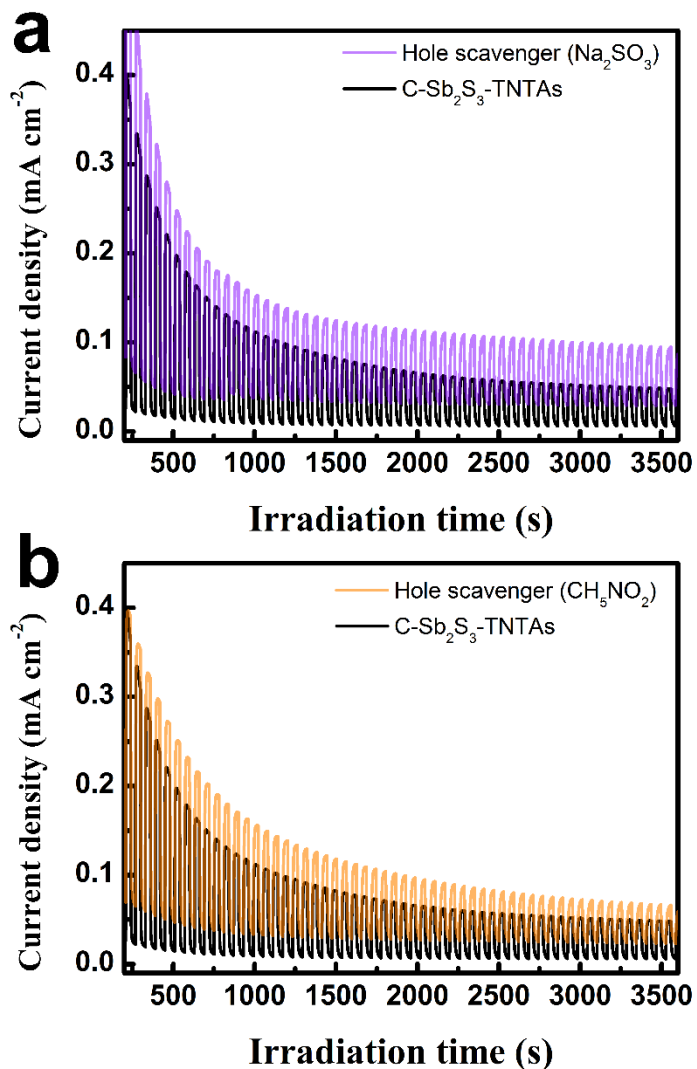
Fig. S22. Photocurrents of C-Sb$_2$S$_3$-TNTAs with and without adding hole scavengers of (a) Na$_2$SO$_3$ and (b) CH$_5$NO$_2$ in the electrolyte at a bias of 1.23 V *vs*. RHE under continuous simulated solar light irradiation.

References

S1. S. Biniak, G. Szymanski, J. Siedlewski, A. Swiatkowski, *Carbon*, 1997, **35**, 1799-1810.

S2. X. M. Wei, H. C. Zeng, *Chem. Mat.*, 2003, **15**, 433-442.

S3. J. Li, S. Tang, L. Lu, H. C. Zeng, *J. Am. Chem. Soc.*, 2007, **129**, 9401-9409.

S4. S. J. Park, K. S. K, A. Mendez, Science, Technology, Applications and Education. Formatex, 2010, 1905-1916.

S5. S. Tazuke, S. Kurihara, H. Yamaguchi, T. Ikeda, *J. Phys. Chem.*, 1987, **91**, 249-251.

S6. M. Pal, N. R. Mathews, X. Mathew, *J. Mater. Res.* 2017, **32**, 530-538.

S7. K. Xiao, Q. Z. Xu, K. H. Ye, Z.Q. Liu, L.M. Fu, N. Li, Y.B. Chen,; Y.Z. Su, *ECS Solid State Lett*, 2013, **2**, 51-54.